JGR Solid Earth

RESEARCH ARTICLE
10.1029/2018JB017181

A Parametric Analysis of Fault Reactivation in the New Madrid Seismic Zone: The Role of Pore Fluid Overpressure

Henri Leclère[1] and **Éric Calais**[1]

[1]Department of Geosciences, Ecole normale supérieure, Université PSL, Paris, France

Key Points:
- We develop a Mohr-Coulomb-based parametric analysis that allows us to determine the most favorable conditions for fault reactivation
- We apply the method to focal mechanism in the New Madrid Seismic Zone and find that pore fluid pressure is required unless faults are weak
- We argue that weak faults are unlikely and propose a triggering mechanism via deep fluids, possibly upwelling from the upper mantle

Supporting Information:
- Supporting Information S1

Correspondence to:
H. Leclère,
henri.leclere@ens.fr

Citation:
Leclère, H., & Calais, É. (2019). A parametric analysis of fault reactivation in the New Madrid Seismic Zone: The role of pore fluid overpressure. *Journal of Geophysical Research: Solid Earth*, *124*, 10,630–10,648. https://doi.org/10.1029/2018JB017181

Received 16 DEC 2018
Accepted 17 JUL 2019
Accepted article online 25 JUL 2019
Published online 29 OCT 2019

Abstract Earthquakes in Stable Continental Regions (SCR), where localized present-day tectonic loading is negligible, remain difficult to explain. The New Madrid Seismic Zone (NMSZ) is a type-locale for such events, with four M>7 events in 1811–1812 and a regional seismicity that continues to this day. Here, we seek to determine the most favorable conditions for fault reactivation in such a context using 33 earthquakes in the 2.1–4.7 magnitude range with well-determined focal mechanisms while accounting for the vertical gradient of differential stress with depth. To do so, we developed a Mohr-Coulomb-based parametric analysis of fault reactivation that allows us to vary the orientation of the principal stresses, the shape ratio of the stress tensor, the fault friction coefficient, the pore fluid overpressure, and the gradient of differential stress with depth. Doing so, we are able to determine the lowest stress perturbation conditions required for fault reactivation. Our results show that the reactivation of the faults studied here requires pore fluid overpressure, unless their friction coefficient is 0.4 or less. We argue that such weak faults are unlikely and favor a triggering mechanism via deep fluids, possibly upwelling from the upper mantle where a low-velocity seismic anomaly could indicate their presence. This mechanism, documented in other intraplate areas, does not require local tectonic stress or strain accumulation to explain seismicity in active intraplate regions, where elastic strain is drawn from a prestressed crust.

1. Introduction

The occurrence of large earthquakes in regions far from plate boundaries, where the vast majority of the Earth's seismic activity takes place, remains poorly understood. Although some stable continental regions (SCR; Johnston, 1989) appear devoid of seismic activity, others show scattered earthquakes with magnitudes sometimes larger than 7, with little to no imprint on the geology and topography. Space geodetic measurements have confirmed that seismically active SCRs involve very low strain rates, less than 0.2 mm/year over characteristic distances of ~1,000 km (Calais et al., 2006; Craig & Calais, 2014; Nocquet, 2012; Tregoning et al., 2013). In the absence of present-day strain accrual, what triggers large earthquakes, as well as swarms or long-tailed aftershock sequences in SCRs is still debated. Frequently recurring swarm seismicity around Novy Kostel in the Czech Republic provides an example of rapid release of stored elastic strain in response to undoubted fluid injection into a fault network in low-permeability rocks (Cox, 2016; Fischer et al., 2014). Man-made fluid injections are also capable of triggering seismicity in areas where there was none, a well-known process linked to the production of oil and gas from tight formations, for example (e.g., Ellsworth et al., 2015; Keranen & Weingarten, 2018). Whether natural pore fluid overpressure is a generic process capable of activating SCR faults in various settings remains an open question.

The New Madrid Seismic Zone (NMSZ) of the central eastern United States is a type-locale for large SCR earthquakes. During the Holocene, the region experienced millennial-scale temporal clustering of earthquakes—including a sequence of four M>7 events between December 1811 and February 1812 (Johnston & Schweig, 1996; Hough et al., 2000; Nuttli, 1973)—interrupted by millennial-scale, seismically quiescent intervals (Holbrook et al., 2006; Tuttle et al., 2002). Seismicity continues today, outlining the 1811–1812 ruptures of the Cottonwood Grove (CWG) and Reelfoot faults (RF; Johnson et al., 2014; Mueller et al., 2004; Figure 1). For some, this current seismicity is the long-term aftershock sequence of the 1811–1812 events, a transient feature that is therefore not indicative of the long-term earthquake potential of the area (Calais & Stein, 2009; Stein & Liu, 2009).

For others, it implies continued tectonic strain buildup and release on favorably oriented faults prone to reactivation (Hurd & Zoback, 2012; Page & Hough, 2014), with localized accrual of tectonic stress at a significant

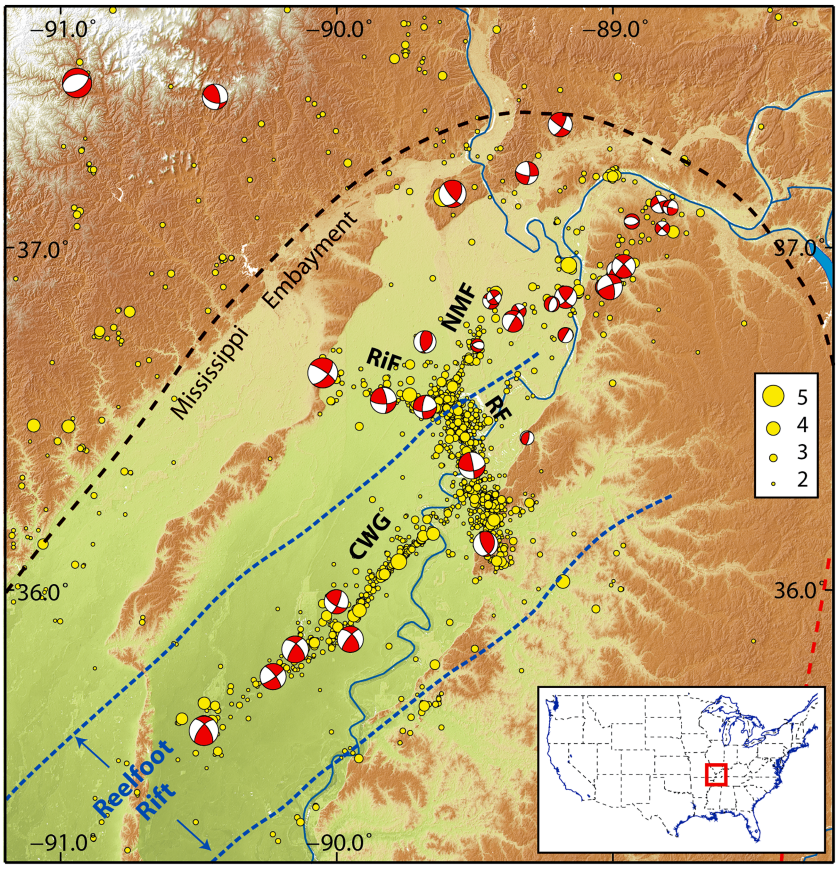

Figure 1. Seismicity map of the New Madrid area, central eastern United States, from 1974 to 2018 shown with yellow dots (CERI, 2018). The focal mechanisms of the 33 events used in this study are shown. The seismicity highlights four major faults: the Reelfoot fault (RF), the New Madrid North (NMN) fault, the Risco fault, and the Cottonwood Grove (CWG) fault. Background color corresponds to elevation.

rate as a result of lateral rheological heterogeneities. Various contributions have been invoked such as a locally weak lower crust (Kenner & Segall, 2000), a locally dense lower crust (Levandowski et al., 2016), or a low-velocity upper mantle (Chen et al., 2014; Pollitz & Mooney, 2014a). Under such conditions, the NMSZ may be able to localize tectonic stress at present if regional-scale displacements are significant (Zhan et al., 2016), which however does not appear to be the case today (Boyd et al., 2015; Craig & Calais, 2014). Alternately, elastic strain energy for recent and future earthquakes may be provided by Glacial Isostatic Adjustment (GIA; Grollimund & Zoback, 2001; Hough & Page, 2011) although different GIA models reach opposite conclusions (Wu & Johnston, 2000). In this view, the NMSZ is equivalent to a very slow plate boundary fault where tectonic and/or GIA strain accrual brings faults to rupture on a recurrent basis, so that its current seismicity is a reliable guide for future large events.

Here, we ask whether earthquakes of the NMSZ with well-determined source mechanisms are triggered by tectonic loading or by local stress perturbations. The quality of the source mechanisms is evaluated from the original publications based on the calculation technique used, the magnitude of the earthquakes, the number of stations used in the calculation, and their azimuthal coverage. We develop a parametric analysis based on the Mohr-Coulomb theory in order to determine the most favorable conditions for fault reactivation, while allowing the magnitude and orientation of the principal stress axes, the coefficient of friction, the pore fluid pressure, and the vertical gradient of the differential stress to vary. Uncertainties on earthquake location and depth are not considered during the parametric analysis. This parametric analysis seeks to improve upon similar studies conducted by fixing most of these parameters to a priori values, including pore fluid pressure (e.g., Hurd & Zoback, 2012; Johnson et al., 2014). The approach outlined below seeks to determine the lowest pore fluid overpressure required to activate NMSZ earthquakes while allowing other parameters to vary.

2. Seismological and Geological Setting

The central eastern United States is underlain by Precambrian terranes welded together to form the North American craton. The Reelfoot rift, which hosts the NMSZ (Braile et al., 1982, 1986), is a northeast trending, 300-km-long, 70-km-wide graben affecting the 1,470-Ma-old Eastern Granite Rhyolite Province (Figure 1; Atekwana, 1996; Csontos & Van Arsdale, 2008; Dart & Swolfs, 1998; Van Schmus et al., 1996). It is part of a network of intracratonic faults resulting from late-stage crustal extension during the breakup of the Rodinia supercontinent and the opening of the Iapetus Ocean in late Precambrian to Cambrian (~565–495 Ma) (Thomas, 2014). During rifting, up to 8 km of Cambrian sediment accumulated in the Reelfoot rift (Csontos & Van Arsdale, 2008).

The Reelfoot rift subsequently underwent compressional tectonics in the late Paleozoic, coincident with the assembly of the Pangea supercontinent (~300 Ma) during the Appalachian orogeny. During these successive episodes of extension and compression, deformation in the Reelfoot rift localized along northeast and northwest striking faults (Csontos et al., 2008; Nelson & Zhang, 1991), sealed by up to 5 km of Paleozoic, Cretaceous, and Tertiary marine sediments topped by an Eocene-Quaternary unconformity in the Mississippi embayment (Van Arsdale, 2000). During most of the Pleistocene, alluvial deposits accumulated within the embayment before a rapid late Pleistocene erosional episode by deglacial melt water at the transition from glacial to interglacial conditions (Rittenour et al., 2007).

The NMSZ is a narrow region of localized seismicity that coincides with the center of the Reelfoot paleo-rift in the upper Mississippi embayment (Figure 1). Seismicity is distributed throughout the upper crust, with a majority of events occurring below 5 km, in the crystalline basement. Seismicity defines a SSW-NNE striking branch associated with the CWG and connects to the north with a broader cluster of events that mark the NW-SE striking RF. The former consistently shows right-lateral strike-slip faulting events, while the latter shows a combination of normal, reverse, strike-slip, and oblique slip mechanisms. Two smaller seismically active segments develop to the northwest, the NNE-SSW trending New Madrid North (NMN) fault and NW-SE trending Risco fault, dominated by right-lateral and left-lateral strike-slip events, respectively (Johnson et al., 2014; Herrmann & Canas, 1978; Shumway, 2008). Overall, the NMSZ is classically interpreted as a right-lateral strike-slip system along the CWG and NMN faults, with a compressive left stepover along the RF.

Crustal and upper mantle structures beneath the NMSZ are well studied, thanks to a number of active and passive seismic experiments. The most notable crustal feature is a high velocity anomaly just above the Moho, interpreted by some as a mafic body, or "rift pillow," that formed during the initiation of the Reelfoot rift (Braile et al., 1982; Hildebrand & Easton, 1995; Mooney et al., 1983). Body wave and surface wave seismic tomography studies consistently show anomalously low seismic velocities in the upper mantle that may sign the presence of deep fluids beneath the NMSZ (Nyamwandha et al., 2016; Pollitz & Mooney, 2014b).

The New Madrid region was struck by four earthquakes of magnitude 7 or greater in 1811–1812 (Johnston & Schweig, 1996; Hough et al., 2000) and is currently undergoing low-level seismic activity, with earthquakes rarely exceeding magnitude 3 (CERI, 2018; Page & Hough, 2014). Although once debated (Calais et al., 2005; Smalley et al., 2005), the current rate of strain accumulation on faults within the NMSZ is undistinguishable from zero, with a 95% confidence upper bound of 0.2 mm/year over about 500 km (Boyd et al., 2015; Craig & Calais, 2014).

Recent research has shown that faults other than the seismically active NMSZ have been active in the Quaternary—possibly the Holocene for some of them—within the broad upper Mississippi embayment region (e.g., Cox et al., 2013; Guo et al., 2014; Hao et al., 2013). The currently seismically active NMSZ is therefore only one of several regional faults that have experienced recent seismic activity. However, none of these other faults appear to be currently seismically active, while current regional seismicity appears to be limited to the fault segments that ruptured in 1811–1812. There is no clear explanation for this observation at the moment, though it may indicate that fault activity is "clustered and migrating" (Crone et al., 1992; 1997; Liu et al., 2011).

The tectonic stress field in the United States is characterized by a lateral transition from horizontal extension in the central eastern United States to horizontal compression in the southeastern Canada (e.g., Hurd &

Zoback, 2012; Levandowski et al., 2018). In the New Madrid region, the tectonic stress field shows a pure strike-slip regime with an ENE-WSW trending maximum horizontal stress (Johnson et al., 2014; Hurd & Zoback, 2012). This is confirmed by a recent stress tensor inversion for the continental United States (Levandowski et al., 2018), which, in addition, shows a broad spatial wavelength variability in the state of stress across the continent.

3. Description of the Parametric Analysis

The NMSZ provides a favorable testing for the exercise described below because of its seismicity level, a good seismic network that allows for the determination of precise focal mechanisms for the largest events, and a relatively simple tectonic setting far from active plate boundaries. The main goal of the parametric analysis presented here is to find the conditions for which faults are most easily reactivated, using fewer a priori hypotheses than previous studies that had a similar objective. Our method is based on the Mohr-Coulomb theory, under which the reactivation of a fault with a given strike and dip is a function of the magnitude and orientation of the principal stresses, the fault coefficient of friction μ_s, the vertical gradient of differential stress k, and the pore fluid pressure. A range of combination of these parameters may obviously allow for fault reactivation. Our approach aims at determining the lowest pore fluid pressure required for reactivation while allowing other parameters to vary.

The major improvement of our analysis over previous studies of fault reactivation is the minimum constraints we impose on the parameters that control fault reactivation. Indeed, we only assume that (1) one of the principal stress axes is vertical, in agreement with Hurd and Zoback (2012), (2) the crust is fully saturated with hydrostatic pore fluid pressure, as justified in Townend and Zoback (2000), and (3) differential stress increases linearly with depth (Streit, 1999). We assume a homogeneous stress field and do not account for the static stress changes associated to large earthquakes such as those of the 1811–1812 New Madrid sequence (Mueller et al., 2004), as their calculation would be too uncertain given the available information. While doing so, we allow the fault friction coefficient and the vertical gradient of differential stress to vary and the nonvertical principal stresses to rotate.

In comparison, the study of Hurd and Zoback (2012), which analyzed the reactivation of 12 focal mechanisms in the NMSZ (see Table 1), assumes that optimally oriented fault planes are reactivated under hydrostatic pore fluid pressure, which implies that the great Mohr circle (σ_1,σ_3) is tangent to the reactivation envelope. This assumption simplifies the analysis by removing the need to quantify differential stress. Also, the local direction of SHmax and SHmin is fixed and the τ/σ_n ratio required for reactivation is computed for a range of strikes and dips by rotating the fault plane within ±45°. This approach therefore determines whether a fault plane is favorably oriented or misoriented within the regional stress field (e.g., Leclère & Fabbri, 2013; Morris et al., 1996). However, it does not provide information on whether the fault is close to reactivation, which depends on the actual value of differential stress and pore fluid pressure at seismogenic depth (e.g., Cox, 2010).

Under the theory of Mohr-Coulomb, slip occurs when the criterion

$$\tau = \mu_s(\sigma_n - P_f) + C \tag{1}$$

is satisfied, with τ and σ_n being, respectively, the shear stress and normal stress applied on the fault, μ_s the coefficient of friction, P_f the pore fluid pressure, and C the fault cohesion. Here we assume cohesionless faults so that C is not part of the following parametric analysis. The New Madrid faults may not be cohesionless, as the very low regional strain rate that should promote healing. However, the stress perturbation required for reactivation is smaller for cohesionless faults (C=0) than for cohesive ones (C>0) as shown in equation (1). Therefore, assuming cohesionless faults contributes to minimizing the stress perturbation required for fault reactivation. In other words, if the New Madrid faults were cohesive, then stress perturbations larger than the ones calculated here would be required for reactivation.

In the case of the NMSZ, we set the intermediate stress axis σ_2 to be vertical and the largest principal stress axis σ_1 to strike N80°E, based on previous regional stress inversions conducted in the study area (Hurd & Zoback, 2012; Johnson et al., 2014; Levandowski et al., 2018). We use a set of 33 earthquake focal mechanisms determined using either waveform modeling (Herrmann, 1979; Herrmann & Ammon, 1997; Hurd &

Table 1
List of the 33 Earthquake Focal Mechanisms Used in This Study

#	Year	Month	Day	Hour	Minute	Second	Latitude	Longitude	Depth (km)	Magnitude	Strike	Dip	Rake	Reference
1	1962	2	2	6	43	0	36.37	89.51	7.5	4.2	350	84	145	Herrmann (1979)
2	1963	3	3	17	30	0	36.64	90.05	15	4.7	304	78	−28	Herrmann and Ammon (1997)
3	1965	8	14	13	13	0	37.22	89.31	1.5	3.6	2	70	−20	Herrmann (1979)
4	1965	10	21	2	4	0	37.48	90.94	5	4.6	260	40	−70	Herrmann (1979)
5	1967	7	21	9	14	0	37.44	90.44	15	4	350	60	135	Herrmann and Ammon (1997)
6	1970	11	17	2	13	0	35.86	89.95	16	4.1	220	75	150	Herrmann (1979)
7	1975	6	13	22	40	0	36.54	89.68	9	3.7	85	60	−20	Herrmann (1979)
8	1976	3	25	0	41	0	35.59	90.48	12	4.6	220	65	150	Herrmann (1979)
9	1990	9	26	13	18	0	37.16	89.58	15	4.28	140	75	50	Herrmann and Ammon (1997)
10	1991	5	4	1	18	0	36.56	89.83	8	4.1	90	67	20	Herrmann and Ammon (1997)
11	1994	2	5	14	55	0	37.36	89.19	16	3.8	30	70	170	Herrmann and Ammon (1997)
12	1996	11	29	0	0	0	35.97	90	11	3.8	120	65	15	Hurd and Zoback (2012)
13	1998	4	8	18	16	49	36.94	88.99	7.62	2.7	24	31	71	Shumway (2008)
14	1998	5	11	8	7	15	36.89	89.03	2.66	2.8	239	83	−1	Shumway (2008)
15	1998	9	17	8	46	41	36.85	89.44	4.6	2.6	291	86	−6	Shumway (2008)
16	1999	5	27	6	0	4	36.72	89.49	4.19	2.1	116	54	−59	Shumway (2008)
17	1999	6	22	7	5	35	36.86	89.43	5.21	2.3	146	86	4	Shumway (2008)
18	1999	7	6	9	29	1	37.06	88.82	4.25	2.3	225	85	1	Shumway (2008)
19	2000	6	27	6	2	57	37.13	88.83	4.19	2.8	246	75	−1	Shumway (2008)
20	2000	8	3	8	53	39	37.12	88.79	5.07	2.4	281	90	35	Shumway (2008)
21	2002	5	7	10	13	54	36.75	89.17	5.56	2.4	300	5	0	Shumway (2008)
22	2002	6	20	2	11	40	36.45	89.31	13.73	2.2	12	70	79	Shumway (2008)
23	2003	6	6	0	0	0	36.89	89.01	0.5	4	250	80	155	Hurd and Zoback (2012)
24	2003	10	18	5	59	46	36.82	89.34	3.6	2.3	330	85	0	Shumway (2008)
25	2004	2	12	6	49	49	37.08	88.93	9.3	2.4	285	42	−71	Shumway (2008)
26	2004	6	15	0	0	0	36.73	89.68	4.5	3.5	175	55	70	Hurd and Zoback (2012)
27	2004	7	16	0	0	0	36.86	89.17	4	3.5	43	71	159	Hurd and Zoback (2012)
28	2005	2	10	0	0	0	35.75	90.23	14	4.1	55	80	−165	Hurd and Zoback (2012)
29	2005	3	15	4	24	18	36.84	89.22	5.43	2.4	198	60	−84	Shumway (2008)
30	2005	5	1	0	0	0	35.83	90.15	8	4.2	315	60	20	Hurd and Zoback (2012)
31	2005	6	2	0	0	0	36.14	89.46	15	3.9	155	65	70	Hurd and Zoback (2012)
32	2005	6	20	0	0	0	36.95	88.96	9	3.7	315	80	10	Hurd and Zoback (2012)
33	2010	3	2	0	0	0	36.79	89.36	5	3.4	211	86	135	Hurd and Zoback (2012)

Zoback, 2012) or first arrivals (Shumway, 2008). Twelve of them were previously analyzed by Hurd and Zoback (2012). These events span the 1962–2010 time interval, with magnitudes ranging from 2.1 to 4.7, and depths ranging from 0.5 to 15 km (Table 1). The use of focal mechanisms requires the identification of the actual fault plane and its auxiliary plane. Here, we conduct the analysis on both nodal planes, then retain the plane that is the most easily reactivated. This serves, again, to minimize the stress perturbation required for fault reactivation.

We compute τ and σ_n using Cauchy's formulae for a range of (1) orientations and magnitudes of the principal stress axes and (2) fault friction coefficient values μ_s. From this, we find the set of parameters under which a given fault plane is most easily reactivated, which we hereafter call the "most favorable condition." The most favorable condition for the reactivation of a cohesionless fault plane has the highest τ/σ_n ratio, which corresponds to the theoretical friction coefficient μ_s^{theo} for reactivation without stress perturbation.

If μ_s^{theo} is equal to or lower than the fault friction μ_s, then no stress perturbation is needed to reactivate the fault. Conversely, if μ_s^{theo} is larger than the friction coefficient μ_s, then a stress perturbation is required for reactivation that corresponds to pore fluid pressure P_f in the Mohr-Coulomb criterion. Here we assume that this stress perturbation is the result of the development of pore fluid overpressure, that is, pore fluid larger than hydrostatic.

The parametric analysis is based on three steps (Figure S1 in the supporting information) that are described below: (1) selection of all the possible stress tensors, described by their shape ratio Φ and the strike of σ_1, which explains the direction and sense of shear along each fault plane, (2) calculation of the maximum differential stress that the fault plane can support before the intact rock fails, and (3) calculation of the pore fluid overpressure required to reactivate the fault plane, if it is needed.

3.1. Step 1: Stress Tensor and Compatible Φ Values

The Φ value of a stress tensor, which describes the position of σ_2 relative to σ_1 and σ_3, is defined by

$$\Phi = \frac{\sigma_2 - \sigma_3}{\sigma_1 - \sigma_3}. \quad (2)$$

For a given fault and given principal stress axes directions, Φ controls the direction and sense of shear (Angelier, 1990; Bott, 1959; Xu et al., 2017).

In this work, we allow the principal stress axis σ_1 to rotate by ±20° about its regional mean strike of N80°E. For each fault plane and direction of σ_1 (from N60°E to N100°E), we compute the direction and sense of shear along the selected fault plane while varying Φ following the method described in Xu et al. (2017). We keep for step 2 the Φ values that explain the observed direction and sense of shear within ±10°. We call them hereafter "compatible Φ values." This ±10° value corresponds to one third of the ±30° value classicaly used in stress inversions, and it took indirectly into account focal mechanisms incertainties (e.g., Delvaux & Sperner, 2003). We choose a lower value because allowing for a value greater than 10 would lead to a wider range of compatible Φ values, then to most favorable conditions that would, in the end, not be in agreement with the initial focal mechanism.

Figure 2 shows as horizontal bars the compatible Φ values for each focal mechanism included in the data set and for three directions of σ_1, N60°, N80°, and N100°. Red bars indicate the range over which stresses are lower than the maximal differential stress that the intact rock can support, as explained below.

3.2. Step 2: Calculation of the Maximum Differential Stress

An increase of differential stress promotes fault reactivation, which, as a result, lowers the pore fluid pressure needed to reactivate misoriented faults (Cox, 2010). However, if the differential stress becomes too high, a new fault optimally oriented within the local stress field will form, preventing the reactivation of misoriented faults (Figures 3a–3d). Therefore, for each fault and for each value of compatible Φ, μ_s, and σ_1 strike, there is a maximum differential stress σ_{Dmax} that allows for fault reactivation before failure of the intact rock.

We use the failure mode diagram proposed by Cox, (2010; Figure 3a) to calculate this maximum differential stress σ_{Dmax}, assuming a constant rock density ρ of 2,600 kg/m^3, a tensile strength T of 17.5 MPa for crystalline rocks corresponding to a cohesion $C=2T$ and a friction coefficient μ_{intact} of 0.75 for the intact rock (mean value of Byerlee's law, Byerlee, 1978), and 0.4 to 0.6 for fault planes. We deliberately choose a maximal value of fault plane friction of 0.6—the lower bond of the Byerlee's law—in order to minimize the pore fluid overpressures required for fault reactivation. Using larger values, up to 0.85, for instance, would lead to pore fluid overpressure estimates larger than the ones calculated here. σ_{Dmax} is the intersection between the reactivation envelope and the failure envelope represented by white dots in Figure 3a. In a Mohr-Coulomb diagram, σ_{Dmax} is reached when the great Mohr circle ($\sigma_1 - \sigma_3$) is tangent to the failure envelope, as shown in Figure 3b.

We then calculate, for each focal mechanism in the data set, the maximum differential stress σ_{Dmax} that corresponds to the range of compatible Φ values obtained in step 1. This is done by (1) computing a diagram similar to Figure 3a for the depth of the event, the direction of σ_1, and the Φ value using the methodology described in Cox (2010), and (2) finding the intersection between the failure envelope (thick black line on Figure 3a) or the hydrostatic condition (horizontal thick gray line on Figure 3a) and the reactivation envelope (thin black lines on Figure 3a). We do this for the range of static fault friction μ_s from 0.4 to 0.6 tested here. The resulting range of σ_{Dmax} is shown with a horizontal bar on Figure 4 for each focal mechanism, as a function of the depth of the event, and for μ_s=0.6.

We assume the differential stress σ_D to increase linearly with depth and test three values of its vertical gradient k derived from borehole stress measurements (Quinones et al., 2018; Streit, 1999): a lower bound

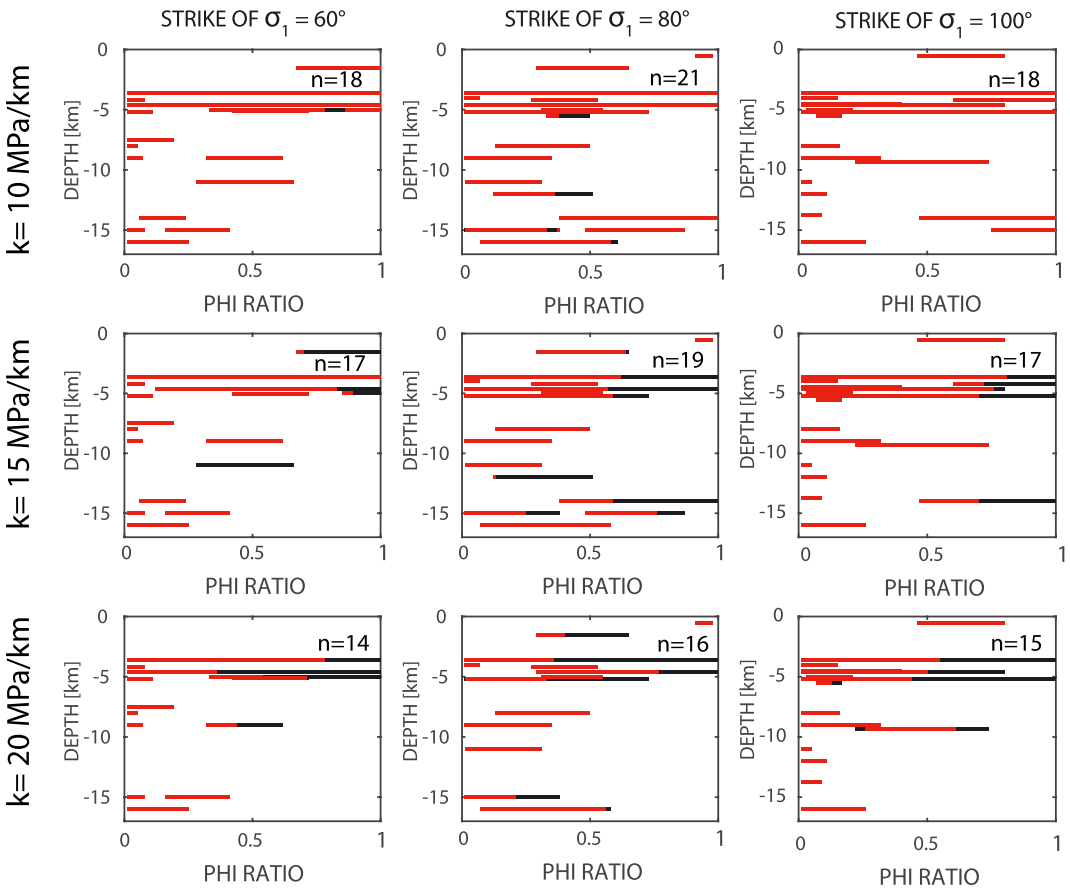

Figure 2. Range of Φ ratio values that explain the observed slip vector for each fault plane with an angular misfit less than 10° and for different strikes of σ_1 (N60° [left column], N80° [middle column], and N100° [right column]). Results shown here use a friction coefficient of 0.6. Red horizontal bars are the Φ values used for the calculation of the pore fluid overpressure on Figure 5. Black horizontal bars are rejected values due to failure of the intact rock before the fault can be reactivated.

value of 10 MPa/km, an intermediate value of 15 MPa/km, and an upper bound value of 20 MPa/km. The thin black lines on each panel of Figure 4 represents the linear evolution of the differential stress σ_D with depth for these three values of k. They define the boundary between the area where the available differential stress is large enough to fracture intact rock, hence preventing fault reactivation, and the area where differential stress allows for fault reactivation before a new fault, optimally oriented within the local stress field, can form.

These two possibilities are coded in red and black on Figure 4: horizontal black bars fall in the area where the available differential stress (for a given k) is larger than the maximum differential stress the rock can sustain before failure of the intact rock, while red bars fall in the area where the available differential stress is lower than this maximum differential stress, hence where reactivation is possible. We only retain for the next step the maximal differential stress values shown in red where σ_{Dmax} is greater than the available differential stress.

3.3. Step 3: Calculation of the Pore Fluid Overpressure

We are now in a position to compute the pore fluid pressure P_f required for fault reactivation by combining Cauchy's formulae and the Mohr-Coulomb criteria. We have at our disposal, for each event in the catalog and for each strike of σ_1, the depth, the available differential stress at that depth (for a given k), and the range of compatible Φ values for that event (red bars on Figures 2).

The Cauchy's formulae provide τ and σ_n as a function of σ_1,σ_2, and σ_3 as follows:

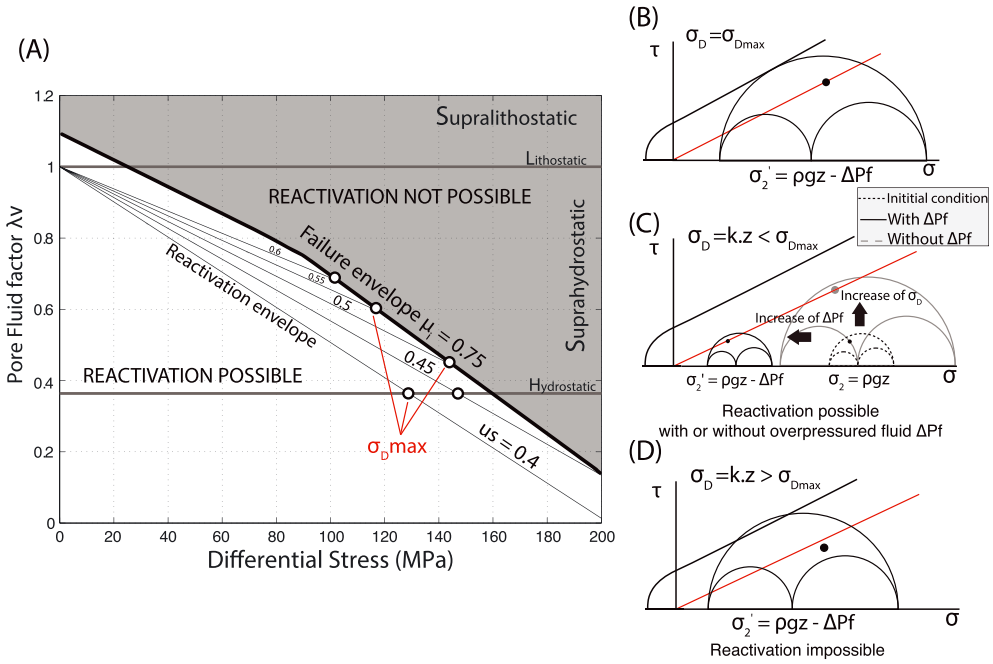

Figure 3. (a) Example of a failure mode diagram, as developed by Cox (2010), which allows us to compute the maximum differential stress that a fault can support before failure of the intact rock. Note that this is a generic example meant to illustrate the principle of failure mode diagrams—its values do not correspond to a specific set of parameters used in this study. Thick black line is the failure envelope of the intact rock, along which new faults would form before reactivation. The thin black lines are the reactivation envelopes for various values of the static coefficient of friction μ_s. The intersections between the reactivation and failure envelopes correspond to the maximum differential stress allowing fault reactivation. We assume the crust is fully saturated at hydrostatic pore fluid pressure, which also limits that maximum differential stress. The five white dots show examples of the maximum differential stress in this example. (b–d) Schematic Mohr diagrams illustrating whether a fault plane can be reactivated. Straight red lines show reactivation envelope, straight black lines show failure envelope. Black dot show the location of a particular fault. (b) The great Mohr circle is tangent to the failure envelope (σ_D=σ_{Dmax}) and the fault is on the reactivation envelope—it is therefore reactivated. (c) The great Mohr circle is initially below the reactivation envelope (dashed circles). Reactivation of the fault requires an increase of pore fluid pressure (black circles) and/or an increase of differential stress (gray circles). (d) The great Mohr circle is above the failure envelope (σ_D>σ_{Dmax}) and the fault is below the reactivation envelope—reactivation is impossible.

$$\tau^2 = (\sigma_1-\sigma_2)^2 l^2 m^2 + (\sigma_2-\sigma_3)^2 m^2 n^2 + (\sigma_3-\sigma_1)^2 l^2 n^2 \tag{3}$$

and

$$\sigma_n = l^2\sigma_1 + m^2\sigma_2 + n^2\sigma_3 \tag{4}$$

where l, m, and n are the direction cosines between the normal to the fault plane n and the principal stresses σ_1, σ_2, and σ_3, respectively.

The magnitude of σ_2 is simply $\rho g z$ where g is the acceleration of gravity and ρ the rock density. The values of σ_1 and σ_3 can then be computed, for a given Φ, using:

$$\sigma_3 = \sigma_2 - \Phi\sigma_D \tag{5}$$

with

$$\sigma_D = k{\cdot}z \tag{6}$$

and

$$\sigma_1 = \sigma_3 + \sigma_D \tag{7}$$

The pore fluid pressure P_f required to reactivate faults can then be computed using equation (1) (with C=0, see above) as

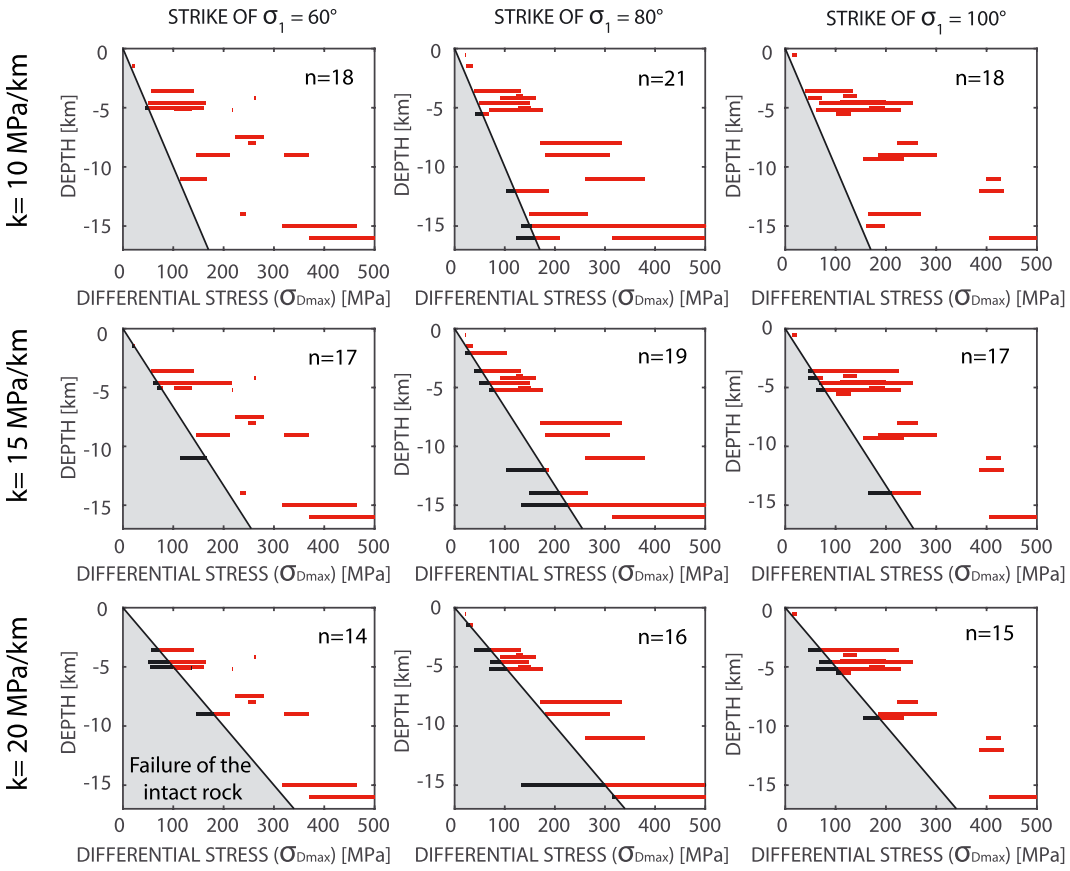

Figure 4. Range of maximal differential stress values σ_{Dmax} before failure of the intact rock for different strikes of σ_1 (N60° [left column], N80° [middle column], and N100° [right column]). Results shown here use a friction coefficient of 0.6. Oblique black lines show the available differential stress as a function of depth assuming three values of the vertical gradient of differential stress k (10, 15, and 20 MPa/km). Horizontal black bars fall in the area where the available differential stress (for a given k) is larger than the maximum differential stress the rock can sustain before failure of the intact rock. Red bars fall in the area where the available differential stress is lower than this maximum differential stress, hence where reactivation is possible. The length of the red bars and the number of planes that can be reactivated n decrease as the vertical gradient of differential stress increases, because large differential stress values can lead to intact rock failure before fault reactivation.

$$P_f = \frac{\mu_s \sigma_n - \tau}{\mu_s} \tag{8}$$

where the fluid overpressure $\Delta P_f = P_f - \rho_{water} g z$.

Figure 5 shows the resulting range of pore fluid overpressure values required to reactivate faults in our data set for three values of σ_1 strike, and vertical gradient of differential stress k. If the lower end of the red bar reaches zero, then fault reactivation does not require pore fluid overpressure for the range of parameters tested here. If it does not, then the lower end of the red bar corresponds to the minimum pore fluid overpressure required for fault reactivation. As one expects, we observe that for a given strike of σ_1, increasing the differential stress gradient k reduces the pore fluid overpressure required to reactivate faults but also decreases the number of planes that can be reactivated before failure of the intact rock.

An alternate representation of this search process is illustrated with Mohr diagrams on Figure 6 for two of the focal mechanisms considered here. The entire data set is shown on supporting information Figure S2. On this figure we use in each case the σ_1 direction that corresponds to the minimum ΔP_f, the upper bound of the differential stress gradient k=20 MPa/km, and a static fault friction μ_s=0.6. Using these parameters, we construct Mohr diagrams for the range of compatible Φ values for each focal mechanism (red bars on Figures 2 and 4). One Mohr diagram corresponds to one fault plane and its compatible Φ values. Figure 6a shows

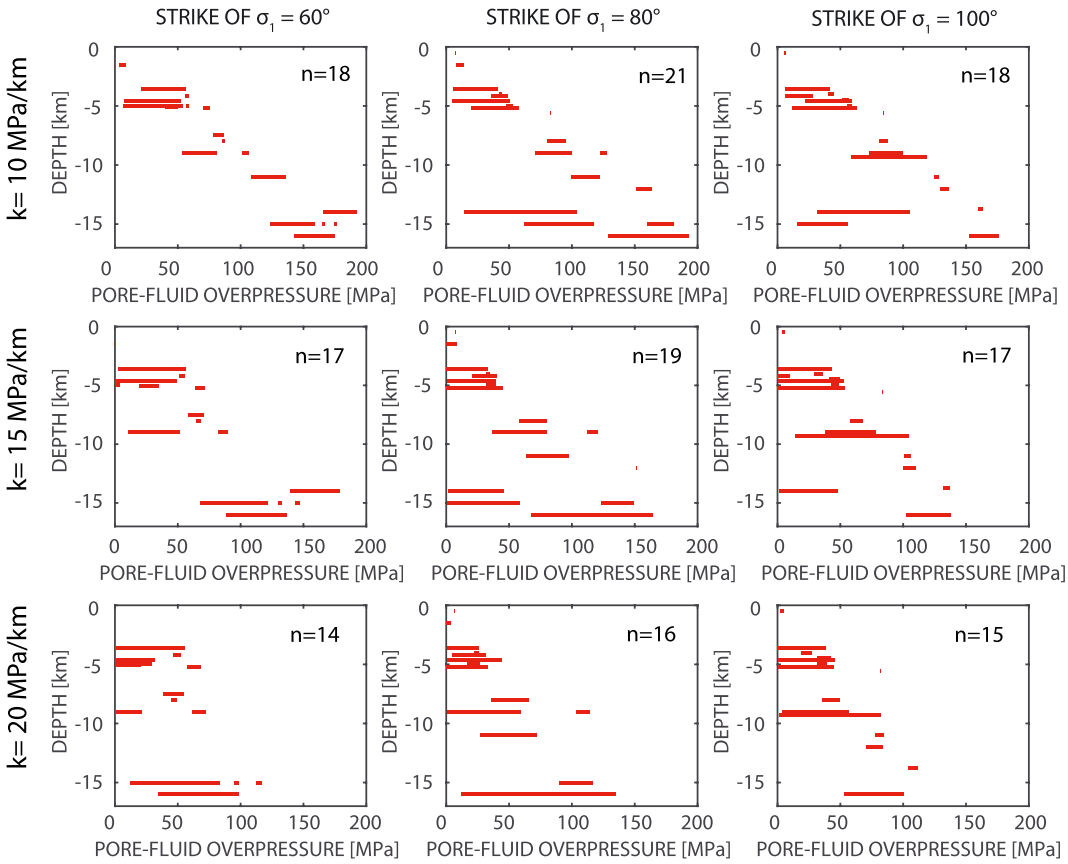

Figure 5. Range of pore fluid overpressure values required to reactivate faults in our data set for three values of σ_1 strike and vertical gradient of differential stress k. Here we only retained the Φ values that allow for fault reactivation, shown by red bars on Figure 2. Results are shown for three different strikes of σ_1 (N60° [left column], N80° [middle column], and N100° [right column]) and three values of the vertical gradient of differential stress k (10, 15, and 20 MPa/km). Results shown here use a friction coefficient of 0.6. An increase of the vertical gradient of differential k lowers the pore fluid overpressure required to reactivate faults. n is the number of fault planes that can be reactivated.

a case where the range of compatible Φ values includes a fault plane in Mohr circle that reaches the reactivation envelope. As the fault plane gets closer to the reactivation envelope, the pore fluid overpressure required for reactivation, shown by a colored dot, decreases to zero. Figure 6b shows a case where the range of compatible Φ values never leads to a fault plane in Mohr circle that reaches the reactivation envelope. As the fault plane gets closer to the reactivation envelope, the pore fluid overpressure required decreases as well but never reaches zero. In that case, the minimum pore fluid overpressure ΔP_f required for reactivation is 84.5 MPa.

4. What Are the Most Favorable Conditions for Reactivation?

We now seek, for each tested value of friction coefficient μ_s and differential stress gradient k, the lowest fluid overpressure value necessary to reactivate each fault plane within the NMSZ source mechanism data set given the range of σ_1 directions tested here. We call this combination of parameters the "most favorable conditions." These conditions correspond to the darkest blue point on each Mohr-Coulomb diagram of Figures 6 and S2.

Figure 7 shows, in map view, the strike of σ_1 and the fluid overpressure value under the most favorable conditions in the case of a 20- and 15-MPa/km differential stress gradient k and a friction coefficient of 0.6, 0.5, and 0.4. We discuss separately below the role of local stress rotations, pore fluid overpressure, and fault friction on fault reactivation.

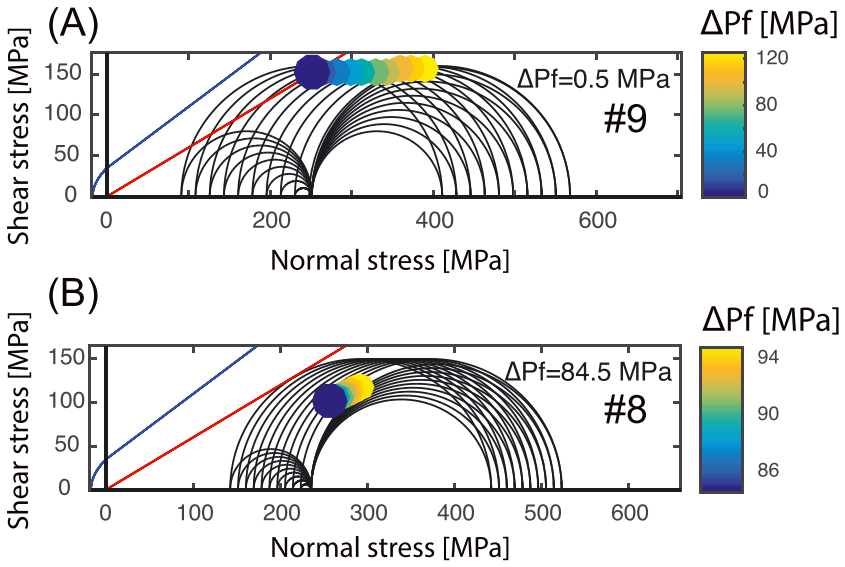

Figure 6. Mohr diagrams for two of the focal mechanisms in the database. Straight red lines show reactivation envelope, blue lines show intact rock failure envelope. For each event, we draw a series of 3-D Mohr circles for the range of compatible Φ values for each focal mechanism (red bars on Figures 2 and 4). This figure uses k=20 MPa/km and μ_s=0.6. (a) The range of compatible Φ values includes a Mohr circle that intersects the reactivation envelope so that reactivation does not require pore fluid overpressure. As the Mohr circle gets closer to the reactivation envelope, the pore fluid overpressure required for reactivation, shown by a colored dot, decreases to zero. (b) The range of compatible Φ values never leads to a Mohr circle that intersects the reactivation envelope. As the Mohr circle gets closer to the reactivation envelope, the pore fluid overpressure required decreases as well but never reaches zero. Here reactivation requires a minimum pore fluid overpressure of 84.5 MPa.

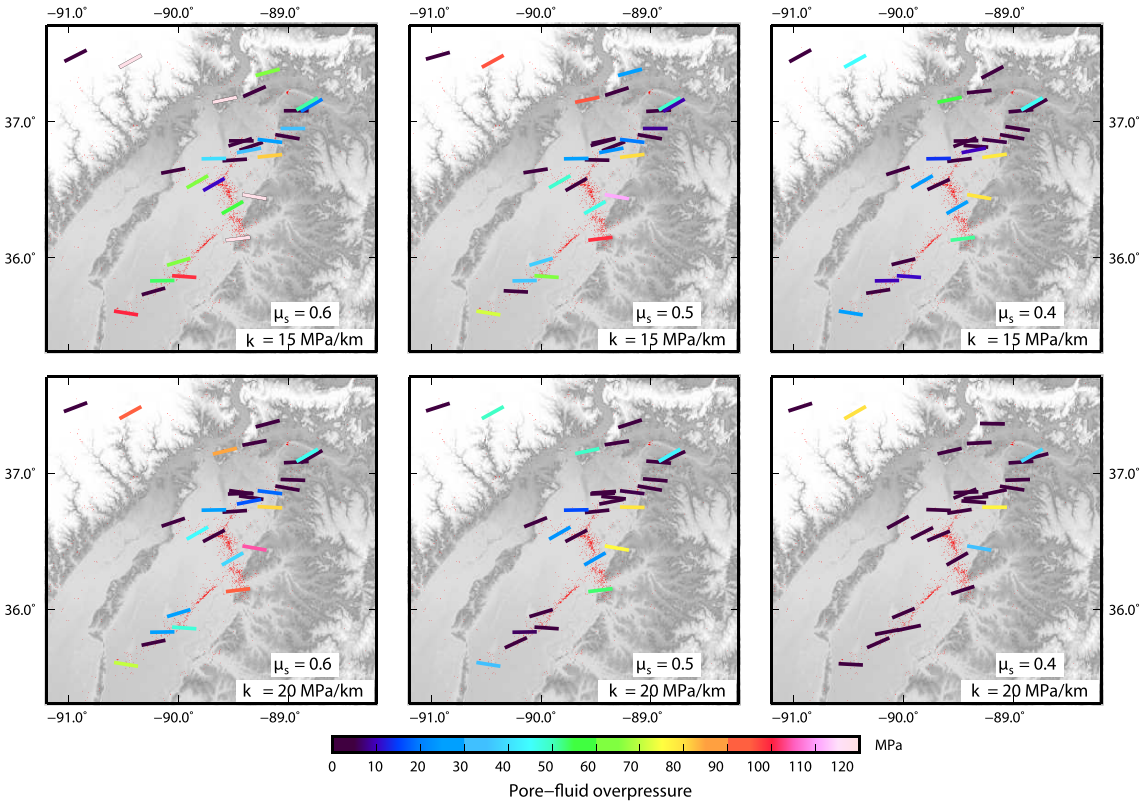

Figure 7. Maps of the σ_1 strike and pore fluid overpressure values ΔPf for the most favorable conditions and three values of the coefficient of friction (μ_s = 0.6 [left column], 0.5 [middle column], and 0.4 [right column]) and for two values of differential stress gradient k (15 [top row] and 20 [bottom row] MPa/km). Bars indicate the strike of σ_1 and colors the magnitude of ΔPf. Location of the New Madrid North Fault, Reelfoot Fault, and Cottonwood Grove Fault are indicated on Figure 1.

4.1. Role of Local Stress Rotations

Figure 7 shows that most of the 33 focal mechanisms used in this study can be reactivated provided that the direction of σ_1 rotates locally in the N60°E to N100°E range. Under these conditions, 29 events can be reactivated for a friction coefficient between 0.6 and 0.4. The four remaining fault planes that are not plotted on Figure 7 have a misfit angle larger than 10° for the range of σ_1 strike and Φ values. The reactivation of these fault planes requires a different stress regime or larger horizontal stress rotation. On Figure 7, the mean σ_1 direction required is approximately ENE-WSW along the Reelfoot (RF) fault and E-W along the CWG and NMN faults.

This does not prove that local stress rotations indeed occur, but illustrates, as expected, that stress rotations promote fault reactivation under the most favorable conditions. Conversely, if local stress rotations were not present, then fault reactivation would require effective stress perturbations—such as pore fluid overpressure—larger than those computed here.

4.2. Role of Pore Fluid Overpressure

Figure 7 shows that pore fluid overpressure up to ~120 MPa is required to reactivate the faults in our data set, regardless of local σ_1 rotations. The total pore fluid pressures can then be compared to the hypocentral depths to see if they fall with the hydrostatic, sublithostatic or lithostatic domains (supporting information Figure S4). To do this, the pore fluid pressures can be converted to pore fluid factor $\lambda_v = P_f/(\rho\, g\, z)$ with sublithostatic maximal values of 0.68, 0.76, and 0.81 for respective k values of 20, 15, and 10 MPa/km and for μ_s equal to 0.6. Among the 29 fault planes, only 14 can be reactivated with a pore fluid overpressure less than 5 MPa for a differential stress increase with depth σ_D of 20 MPa/km and for a fault friction coefficient of 0.6, the lower limit of Byerlee's law (Figure 8a). These fault planes are distributed between the CWG, RF, and NM faults except two fault planes located further west of the NMN. This number decreases to 10 and 4 when the vertical differential stress gradient k drops, respectively, to 15 and 10 MPa/km (Figures 7, 8b, and 8c). A similar behavior can also be observed when considering the pore fluid factor λ_v, with lower pore fluid factor values required for reactivation when friction coefficient μ_s and increase of differential stress with depth k are lowered (Figures 8d–8f).

Larger friction coefficients, not tested here but consistent with the 0.6–0.85 range of Byerlee's law and cohesive faults ($C>0$) would require even larger pore fluid overpressure for fault reactivation.

4.3. Role of Fault Friction Coefficient

If weak minerals such as clays are present within faults, their static coefficient of friction μ_s can drop below 0.6 (Behnsen & Faulkner, 2012; Moore & Lockner, 2004). Figures 7 and 8 show that a reduction of μ_s lowers the pore fluid overpressure required for fault reactivation and also increases the number of fault planes that can be reactivated with pore fluid overpressure lower than 5 MPa. With a friction coefficient of 0.5 and a differential stress gradient k of 20 MPa/km, the fault planes that can be reactivated with low pore fluid overpressure (<5 MPa) are preferentially located along the CWG and NMN faults rather than on the RF fault (Figure 7). Faults in the RF area thus appear to be the strongest but still need pore fluid overpressure to be reactivated, even for a coefficient of friction as low as 0.5. For an even lower friction coefficient of 0.4 and for a differential stress gradient k of 20 MPa/km, all but four fault planes can be reactivated with a pore fluid overpressure lower than 5 MPa, as shown on Figures 7 and 8.

To further illustrate how a reduction of the static coefficient of friction μ_s promotes fault reactivation, we sort the 29 fault planes into three categories based on their reactivation pore fluid overpressure values from Figure 7: (i) low overpressure, 0 to 5 MPa, (ii) intermediate overpressure, 5 to 30 MPa, and (iii) high overpressure, above 30 MPa. We show on Figure 8 how the number of reactivated fault planes varies as a function of friction for three values of gradient of differential stress. For k=10 MPa/km, a decrease of the coefficient of friction does not significantly facilitate the reactivation of fault planes that require intermediate pore fluid overpressure and low pore fluid overpressure, in particular when μ_s<0.55. For a larger vertical gradient of differential stress k, a decrease of the coefficient of friction facilitates the reactivation of fault planes that require low pore fluid overpressure, with an opposite effect—for k=20 MPa/km—on the planes requiring high and intermediate pore fluid overpressure. A reduction of friction on fault reactivation is therefore more

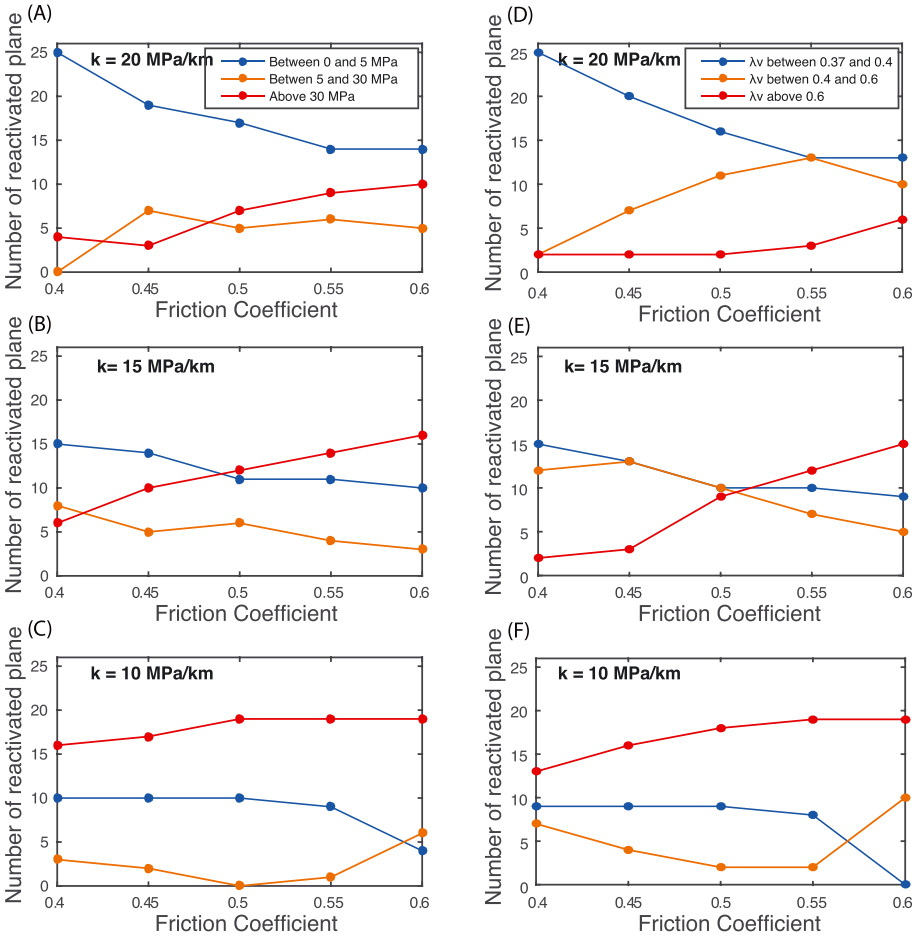

Figure 8. Effects of the reduction of the friction coefficient on fault reactivation. Fault planes are sorted into three categories: (i) low pore fluid overpressure ($0<\Delta P_f<5$ MPa or $0.37<\lambda_v<0.4$), (ii) intermediate pore fluid overpressure ($5<\Delta P_f<30$ MPa or $0.4<\lambda_v<0.6$), (iii) high pore fluid overpressure ($\Delta P_f>30$ MPa or $\lambda_v>0.6$). (a–c) Evolution of pore-fluid overpressure when changing friction coefficient. (d–f) Evolution of pore-fluid factor λv when changing friction coefficient. See explanations in the text.

effective for high values of differential stress gradient. However, we do not observe a fault friction threshold under which fault reactivation would be strongly reduced.

5. Discussion

5.1. Why Are Low Friction or Fluid Overpressure Necessary?

The parametric analysis described above shows that the reactivation of faults without pore fluid overpressure in our data set is possible but not easy, as it requires local σ_1 rotations of ±20°, a large vertical gradient of differential stress k (at least 20 MPa/km), and weak faults (friction coefficient lower than 0.6). Unless those conditions are met together, the reactivation of most faults in our data set requires pore fluid overpressure.

These results differ from those of Hurd and Zoback (2012), who analyzed the reactivation of 12 focal mechanisms also included in our analysis (Table 1), but concluded that shear failure on the preferred nodal planes did not generally require reduced fault friction or elevated pore fluid pressure. This difference stems from their hypothesis that the great Mohr circle ($\sigma_1-\sigma_3$) is always tangent to the reactivation envelope. This assumption, inherited from the so-called "slip-tendency" method (Leclère & Fabbri, 2013; Morris et al., 1996), allows one to fix the position of the fault plane in the Mohr space, hence avoiding a priori knowledge of differential stress. Within this stress state where differential stress is, de facto, fixed, one can then readily describe fault planes as well oriented or misoriented (Sibson, 1985). Using the 3-D fault reactivation model developed by Leclère and Fabbri (2013), we show that more than 60% of the fault planes are favorably

oriented for reactivation with a static friction coefficient of 0.6 (supporting information Figure S3). However, the reactivation of an optimally oriented fault also depends on the differential stress—an optimally oriented fault under a constant magnitude σ_1 gets closer to reactivation as differential stress increases (e.g., Cox, 2010; Leclère & Fabbri, 2013). Our approach does not negate that conducted by Hurd and Zoback (2012) but goes one step further by removing the constraint that the differential stress is always such that rupture will occur. Lifting this constraint shows that the effect of reduced friction or pore fluid overpressure can actually be important to promote fault reactivation.

Stress inversions performed by Johnson et al. (2014) in the NMSZ from focal mechanisms report σ_1 striking N70°E along the NMN and the RF faults, rotating clockwise to N97°E along the CWG fault. These orientations are similar to the best strike of σ_1 for reactivating the RF and CWGs in the most favorable conditions as described above (Figure 7). Their results, however, differ for the NMN, where the most favorable conditions from our work have σ_1 striking E-W. That σ_1 is not consistent with the most favorable conditions implies that stress perturbations larger than those estimated in this study are required to reactivate faults in the NMN region.

5.2. Which of Low Friction or Fluid Overpressure Is More Likely?

We showed that the reactivation of the NMSZ faults with minimum stress perturbations requires a static friction coefficient as low as 0.4. Most hypocenters in the NMSZ are deeper than 5 km, implying that earthquakes occur in the granitic basement, where Byerlee's law implies friction values of at least 0.6. Lower friction values in similar settings are typically found in fault core-zone rich in phyllosilicates such as smectite, chlorite, or montmorillonite (Behnsen & Faulkner, 2012; Moore & Lockner, 2004). The current seismicity in the NMSZ likely results from the reactivation of preexisting shear zones that formed during the complex tectonic history of the North American craton and Reelfoot paleo-rift. Their metamorphic history, together with their role as preferential fluid-pathways that enhance fluid-rock interactions, may have enriched these fault zones in phyllosilicates, in particular, as a result of the alteration of feldspars (Buatier et al., 2012; Boullier et al., 2004; Bistacchi et al., 2012).

However, the friction of phyllosilicates increases with temperature such that values lower than 0.6 are only possible at shallow depth (<10 km; Boulton et al., 2014; den Hartog & Spiers, 2013; Shimamoto, 1986). For instance, experiments conducted on fault gouge from the Alpine fault containing more than 30% of phyllosilicates show an increase of the friction coefficient from 0.4 at room temperature to 0.7 at 210° C, corresponding to a depth of ~10 km assuming a geothermal gradient of ~20° C /km (Blackwell et al., 2011; Boulton et al., 2014). It is therefore unlikely that the NMSZ can be weak (friction of 0.4 or less) at depths greater than ~5 km, where most of the seismicity occurs. In addition, the granitic basement of the NMSZ excludes the presence of very weak minerals such as serpentine or talc, which may explain the low friction and weak behavior of other faults such as the creeping section of the San Andreas fault (Moore & Rymer, 2007).

If NMSZ faults are not weak, then pore fluid overpressures are required for their reactivation. The presence of pore fluid overpressure in the NMSZ is consistent with several independent recent studies. Bisrat et al. (2012) shows swarm clusters and repeating earthquakes clusters in the crystalline basement, with recurrence that requires that the causative faults are weakened and reactivated over short time intervals. In the absence of magma movement or evidence for aseismic creep, the most likely mechanism for earthquake recurrence is pore fluid buildup within the highly fractured Precambrian crust. Two three-dimensional *P* and *S* wave velocity models (Powell et al., 2010; Dunn et al., 2013) show local high V_P/V_S ratios coincident with the RF, at depth greater than 5 km—hence, in the crystalline basement—that these authors interpret as indicative of high pore pressure and/or water-filled microcracks. Shear wave splitting measurements from local seismic data show a higher normalized time delays along the RF compare to the New Madrid region (Martin et al., 2014). These authors also interpret these results as indicative of high cracks densities and high pore fluid pressure.

5.3. How May Fluid Overpressure Build Up?

Several mechanisms have been proposed to explain pore fluid pressure buildup in continental regions. For instance, fluctuations of meteoric water height at depth has been shown to trigger seismicity through pressure diffusion (Bollinger et al., 2007, 2007; Hainzl et al., 2006; Rigo et al., 2008). This mechanism, however, requires high topographic relief to act as a loading column overpressurizing meteoric water downward into

the valleys. This mechanisms is unlikely to be efficient to develop suprahydrostatic pore fluid pressure in a flat region such as the Mississippi plain. Alternatively, surface hydrological loading can induce elastic stresses up to a few kilopascals at seismogenic depths, explaining the annual and multiannual seismicity pattern in the rate of microearthquakes in the NMSZ (Costain, 2008; Craig et al., 2017), but such values are very small compared to the few MPa of pore fluid overpressure documented above.

Pore fluid pressure can also mechanically build up in low-permeability fault patches through a combination of compaction (i.e., porosity decrease) and sealing (i.e., permeability decrease), a process called "creep compaction" (Blanpied et al., 1992; Byerlee, 1990; Sleep & Blanpied, 1992). The three large-magnitude earthquakes that struck the New Madrid region in 1811–1812 likely produced significant fracturing and dilatation in the host rocks. The compaction of pores and cracks associated with fault healing that followed may have induced pore fluid overpressure. However, seismological and hydrogeological surveys following large earthquakes, as well as rock mechanics experiments, show that fault healing starts within the few months following large earthquakes (Li et al., 1998; Xue et al., 2013) and that the healing rate decreases with the regional strain rate (Marone, 1998). Creep compaction driven by afterslip following the 1811–1812 *M*7 earthquakes might have built up pore fluid pressure and triggered seismicity during a few years. However, the efficiency of creep compaction to quasi-permanent trigger seismicity up till today in this tectonically stable region is more questionable.

Upwelling fluids released from depth can also overpressurize faults and trigger seismicity at the intersection of faults, as documented especially in magmatically active areas (Cappa et al., 2009; Heuer et al., 2006; Rice, 1992; Yukutake et al., 2011) but also in the northern Alpine foreland (Deichmann, 1992), and beneath the Flinders Ranges of southeast Australia (Balfour et al., 2015). In this latter case, the authors argued for a deep fluid source from a remnant hydrated mantle on the basis of elevated $^{3}He/^{4}He$ ratios in springs, as also observed in the West Bohemia intraplate seismicity area of Central Europe (Bräuer et al., 2009; Weise et al., 2001). On the other hand, many geological, geochemical, and seismological studies have shown that the root of faults below the brittle/viscous transition is a complex zone with sublithostatic to near lithostatic pore fluid pressure (Han et al., 2016; Küster & Stöckhert, 1999; Leclère et al., 2014; Sibson, 2014; Thomas et al., 2009). It has been proposed that the release of these pressurized fluids from the viscous layer into the brittle crust may trigger cyclic seismic sequences (Thomas et al., 2009; Wehrens et al., 2016).

A similar mechanism may hold for the NMSZ to explain the significant pore fluid overpressure that appears to be required to activate faults in the upper crust. The upwelling fluids would need to originate from a reservoir located deeper than the maximum hypocentral depth of 15 km. The Reelfoot rift and the major faults composing the NMSZ (NMN, RF, and CWG) may act as preferential pathways for deep fluids, as documented in Vogtland/western Bohemia, where mantle fluid upwellings and seismicity are localized near the crossing between the Eger rift and the Mariánské Lazné fault (Bräuer et al., 2009; Weise et al., 2001). Such deep fluids may be metamorphic in origin, for instance, brine water in equilibrium with the granitic basement rocks (Bräuer et al., 2009; Mittempergher et al., 2014), or mantle fluids such as documented along some intraplate faults (Balfour et al., 2015; Kennedy & Soest, 2007). Seismic tomography from surface waves as well as *P* and *S* body waves show a pronounced low-velocity anomaly in the upper mantle beneath the NMSZ extending down to 200–250 km (Chen et al., 2014; Nyamwandha et al., 2016; Pollitz & Mooney, 2014b). On the basis of a comparison with the North China craton, Chen et al. (2014) and Nyamwandha et al. (2016) interpret this low-velocity anomaly as indicative of hot volatiles upwellings from a flat slab segment stalled in the transition zone below the Central United States. Alternatively, Pollitz and Mooney (2014b) proposed that this low-velocity anomaly reflects metasomatic mineral transformations promoted by fluids that emanated from the Bermuda hot spot as it passed beneath the Mississippi Embayment ca. 100 Ma. If such deep fluids are indeed present, pervasive faulting and fracturing throughout the crust of the Reelfoot paleo-rift may act as pathways of increased permeability (Thomas & Powell, 2017) that collect and channel these fluids from the mantle and the lower crust into the brittle crust, where pore fluid overpressure develop, episodically triggering seismic events or swarms.

6. Conclusion

The Mohr-Coulomb-based parametric analysis of fault reactivation described here, applied to 33 NMSZ earthquakes in the 2.1–4.7 magnitude range with well-determined focal mechanisms, shows that these

events required pore fluid overpressure, unless NMSZ faults are particularly weak (static friction coefficient < 0.4). An important aspect of the method is that it accounts for the evolution of differential stress with depth, whereas other analyses of fault reactivation assume that differential stress is always sufficient for reactivation of the optimally oriented fault plane. This explains why our conclusion differs, for example, from that of Hurd and Zoback (2012). We agree with these authors that most preferred nodal planes in this study are favorably oriented for shear failure in the local stress field, but argue that accounting for differential stress with depth is essential as it significantly influences the amount of fluid overpressure—or the value of static fault friction—needed to reactivate faults.

In our view, although phyllosilicates may be present within fault zones throughout the quartzo-feldspathic crystalline basement of the upper Mississippi embayment as a result of fluid-rock interactions, their friction increases with temperature so that values less than 0.6 are unlikely below 5 km, where most of the NMSZ seismicity takes place. We therefore favor a triggering mechanism via the upwelling of deep fluids, possibly originating from the upper mantle, that build sublithostatic to lithostatic overpressure below the brittle-viscous transition and episodically trigger events or swarms as they migrate through the upper crust.

A similar mechanism has been documented in other intraplate seismicity areas such as the Vogtland region of NW Bohemia in Europe where seismic swarms show diffusion-like time migration (e.g., Bräuer et al., 2009; Weise et al., 2001), or the Flinders Ranges in SE Australia where seismicity is likely related to the migration of mantle fluids (e.g., Balfour et al., 2015). A M_w6.5 intraplate earthquake that struck Bostwana in April 2017 was also shown to require deep fluid overpressure (Gardonio et al., 2018). Under such a mechanism, intraplate seismicity does not require localized, present-day, tectonic stress or strain accumulation, contrary to plate boundary events resulting from the near-fault accrual of stress imposed by plate motion (Calais et al., 2016). If the continental crust is able to store elastic energy (i.e., reversible strain on long timescales Craig et al., 2016; Feldl & Bilham, 2006), then short-term fault strength transients, such as those triggered by fluids leaking from the upper mantle, may trigger SCR seismicity, including large events.

Acknowledgments
The data used are listed in the references and figures and are available at https://zenodo.org/deposit/2660086 and also upon request from H. L. H. L. acknowledges postdoctoral support from the École Normale Supérieure. This work was supported by the École Normale Supérieure and the Institut Universitaire de France. We thank Heather DeShon, Stephen Cox, and three anonymous reviewers for constructive comments that significantly helped improve this manuscript.

References

Angelier, J. (1990). Inversion of field data in fault tectonics to obtain the regional stressIII. A new rapid direct inversion method by analytical means. *Geophysical Journal International*, *103*(2), 363–376. https://doi.org/10.1111/j.1365-246X.1990.tb01777.x

Atekwana, E. A. (1996). Precambrian basement beneath the central Midcontinent United States as interpreted from potential field imagery, *Special Paper 308: Basement and basins of eastern North America* (Vol. 308, pp. 33–44). Geological Society of America. https://doi.org/10.1130/0-8137-2308-6.33

Balfour, N. J., Cummins, P. R., Pilia, S., & Love, D. (2015). Localization of intraplate deformation through fluid-assisted faulting in the lower-crust: The Flinders Ranges, South Australia. *Tectonophysics*, *655*, 97–106. https://doi.org/10.1016/j.tecto.2015.05.014

Behnsen, J., & Faulkner, D. R. (2012). The effect of mineralogy and effective normal stress on frictional strength of sheet silicates. *Journal of Structural Geology*, *42*, 49–61. https://doi.org/10.1016/j.jsg.2012.06.015

Bisrat, S., DeShon, H. R., & Rowe, C. (2012). Microseismic swarm activity in the New Madrid Seismic Zone. *Bulletin of the Seismological Society of America*, *102*(3), 1167–1178. https://doi.org/10.1785/0120100315

Bistacchi, A., Massironi, M., Menegon, L., Bolognesi, F., & Donghi, V. (2012). On the nucleation of non-Andersonian faults along phyllosilicate-rich mylonite belts. *Geological Society, London Special Publications*, *367*(1), 185–199. https://doi.org/10.1144/SP367.13

Blackwell, D., Richards, M., Frone, Z., Batir, J., Ruzo, A., Dingwall, R., & Williams, M. (2011). Temperature-at-depth maps for the conterminous U.S. and geothermal resource estimates. *Geothermal Resources Council Transactions*, *35*, 1545–1550.

Blanpied, M. L., Lockner, D. A., & Byerlee, J. D. (1992). An earthquake mechanism based on rapid sealing of faults. *Nature*, *358*(6387), 574–576. https://doi.org/10.1038/358574a0

Bollinger, L., Perrier, F., Avouac, J., Sapkota, S., Gautam, U., & Tiwari, D. R. (2007). Seasonal modulation of seismicity in the Himalaya of Nepal. *Geophysical Research Letters*, *34*, L08304. https://doi.org/10.1029/2006GL029192

Bott, M. H. P. (1959). The mechanics of oblique slip faulting. *Geological Magazine*, *96*(2), 109–117. https://doi.org/10.1017/S0016756800059987

Boullier, A.-M., Fujimoto, K., Ohtani, T., Roman-Ross, G., Lewin, E., Ito, H., et al. (2004). Textural evidence for recent co-seismic circulation of fluids in the Nojima fault zone, Awaji Island, Japan. *Tectonophysics*, *378*(3-4), 165–181. https://doi.org/10.1016/j.tecto.2003.09.006

Boulton, C., Moore, D. E., Lockner, D. A., Toy, V. G., Townend, J., & Sutherland, R. (2014). Frictional properties of exhumed fault gouges in DFDP-1 cores, Alpine Fault, New Zealand. *Geophysical Research Letters*, *41*, 356–362. https://doi.org/10.1002/2013GL058236

Boyd, O. S., Smalley, R., & Zeng, Y. (2015). Crustal deformation in the New Madrid Seismic Zone and the role of postseismic processes. *Journal of Geophysical Research: Solid Earth*, *120*, 5782–5803. https://doi.org/10.1002/2015JB012049

Braile, L. W., Hinze, W. J., Keller, G. R., Lidiak, E. G., & Sexton, J. L. (1986). Tectonic development of the New Madrid rift complex, Mississippi embayment, North America. *Tectonophysics*, *131*(1), 1–21. https://doi.org/10.1016/0040-1951(86)90265-9

Braile, L. W., Keller, G. R., Hinze, W. J., & Lidiak, E. G. (1982). An ancient rift complex and its relation to contemporary seismicity in the New Madrid Seismic Zone. *Tectonics*, *1*(2), 225–237. https://doi.org/10.1029/TC001i002p00225

Bräuer, K., Kämpf, H., & Strauch, G. (2009). Earthquake swarms in nonvolcanic regions: What fluids have to say. *Geophysical Research Letters*, *36*, L17309. https://doi.org/10.1029/2009GL039615

Buatier, M. D., Chauvet, A., Kanitpanyacharoen, W., Wenk, H. R., Ritz, J. F., & Jolivet, M. (2012). Origin and behavior of clay minerals in the Bogd fault gouge, Mongolia. *Journal of Structural Geology*, *34*, 77–90. https://doi.org/10.1016/j.jsg.2011.10.006

Byerlee, J. (1978). Friction of rocks. *Pure and Applied Geophysics*, *116*(4–5), 615–626. https://doi.org/10.1007/BF00876528

Byerlee, J. (1990). Friction, overpressure and fault normal compression. *Geophysical Research Letters*, *17*(12), 2109–2112. https://doi.org/10.1029/GL017i012p02109

CERI (2018). New Madrid earthquake catalog, Center for Earthquake Research and Information. Online; accessed on 2018-11-22.

Calais, E., Camelbeeck, T., Stein, S., Liu, M., & Craig, T. J. (2016). A new paradigm for large earthquakes in stable continental plate interiors. *Geophysical Research Letters*, *43*, 10,621–10,637. https://doi.org/10.1002/2016GL070815

Calais, E., Han, J. Y., DeMets, C., & Nocquet, J. M. (2006). Deformation of the North American plate interior from a decade of continuous GPS measurements. *Journal of Geophysical Research*, *111*, B06402. https://doi.org/10.1029/2005jb004253

Calais, E., Mattioli, G., DeMets, C., Nocquet, J.-M., Stein, S., Newman, A., & Rydelek, P. (2005). Seismology: Tectonic strain in plate interiors? *Nature*, *438*(7070), E9–E10. https://doi.org/10.1038/nature04428

Calais, E., & Stein, S. (2009). Time-variable deformation in the New Madrid Seismic Zone. *Science*, *323*, 1442–1442.

Cappa, F., Rutqvist, J., & Yamamoto, K. (2009). Modeling crustal deformation and rupture processes related to upwelling of deep CO_2-rich fluids during the 1965–1967 Matsushiro earthquake swarm in Japan. *Journal of Geophysical Research*, *114*, B10304. https://doi.org/10.1029/2009JB006398

Chen, C., Zhao, D., & Wu, S. (2014). Crust and upper mantle structure of the New Madrid Seismic Zone: Insight into intraplate earthquakes. *Physics of the Earth and Planetary Interiors*, *230*, 1–14.

Costain, J. K. (2008). Intraplate seismicity, hydroseismicity, and predictions in hindsight. *Seismological Research Letters*, *79*(4), 578–589. https://doi.org/10.1785/gssrl.79.4.578

Cox, S. F. (2010). The application of failure mode diagrams for exploring the roles of fluid pressure and stress states in controlling styles of fracture-controlled permeability enhancement in faults and shear zones. *Geofluids*, *10*(1-2), 217–233. https://doi.org/10.1111/j.1468-8123.2010.00281.x

Cox, S. F. (2016). Injection-driven swarm seismicity and permeability enhancement: Implications for the dynamics of hydrothermal ore systems in high fluid-flux, overpressured faulting regimes—An invited paper. *Economic Geology*, *111*(3), 559–587. https://doi.org/10.2113/econgeo.111.3.559

Cox, R. T., Van Arsdale, R., Clark, D., Hill, A., & Lumsden, D. (2013). A revised paleo-earthquake chronology on the southeast Reelfoot Rift margin near Memphis, Tennessee. *Seismological Research Letters*, *84*(2), 402–408.

Craig, T. J., & Calais, E. (2014). Strain accumulation in the New Madrid and Wabash Valley seismic zones from 14 years of continuous GPS observation. *Journal of Geophysical Research: Solid Earth*, *119*, 9110–9129. https://doi.org/10.1002/2014JB011498

Craig, T. J., Calais, E., Fleitout, L., Bollinger, L., & Scotti, O. (2016). Evidence for the release of long-term tectonic strain stored in continental interiors through intraplate earthquakes. *Geophysical Research Letters*, *43*, 6826–6836. https://doi.org/10.1002/2016GL069359

Craig, T. J., Chanard, K., & Calais, E. (2017). Hydrologically-driven crustal stresses and seismicity in the New Madrid Seismic Zone. *Nature Communications*, *8*(1), 2143. https://doi.org/10.1038/s41467-017-01696-w

Crone, A. J., Machette, M. N., & Bowman, J. R. (1992). Geological investigations of the 1988 Tennant Creek, Australia, earthquakes; implications for paleoseismicity in stable continental regions, U.S. *Geological Survey Bulletin*, *2032-A*, 46.

Crone, A. J., Machette, M. N., & Bowman, J. R. (1997). Episodic nature of earthquake activity in stable continental regions revealed by palaeoseismicity studies of Australian and North American quaternary faults. *Australian Journal of Earth Sciences*, *44*(2), 203–214.

Csontos, R., & Van Arsdale, R. (2008). New Madrid Seismic Zone fault geometry. *Geosphere*, *4*(5), 802–813. https://doi.org/10.1130/GES00141.1

Csontos, R., Van Arsdale, R., Cox, R., & Waldron, B. (2008). Reelfoot Rift and its impact on quaternary deformation in the central Mississippi River valley. *Geosphere*, *4*(1), 145–158. https://doi.org/10.1130/GES00107.1

Dart, R. L., & Swolfs, H. S. (1998). Contour mapping of relic structures in the Precambrian basement of the Reelfoot Rift, North American midcontinent. *Tectonics*, *17*(2), 235–249. https://doi.org/10.1029/97TC03551

Deichmann, N. (1992). Structural and rheological implications of lower-crustal earthquakes below Northern Switzerland. *Physics of the Earth and Planetary Interiors*, *69*(3-4), 270–280. https://doi.org/10.1016/0031-9201(92)90146-M

Delvaux, D., & Sperner, B. (2003). New aspects of tectonic stress inversion with reference to the TENSOR program. *Geological Society, London, Special Publications*, *212*(1), 75–100. https://doi.org/10.1144/GSL.SP.2003.212.01.06

den Hartog, S. A. M., & Spiers, C. J. (2013). Influence of subduction zone conditions and gouge composition on frictional slip stability of megathrust faults. *Tectonophysics*, *600*, 75–90. https://doi.org/10.1016/j.tecto.2012.11.006

Dunn, M., DeShon, H. R., & Powell, C. A. (2013). Imaging the New Madrid Seismic Zone using double-difference tomography. *Journal of Geophysical Research: Solid Earth*, *118*, 5404–5416. https://doi.org/10.1002/jgrb.50384

Ellsworth, W. L., Llenos, A. L., McGarr, A. F., Michael, A. J., Rubinstein, J. L., Mueller, C. S., et al. (2015). Increasing seismicity in the U. S. midcontinent: Implications for earthquake hazard. *The Leading Edge*, *34*(6), 618–626. https://doi.org/10.1190/tle34060618.1

Feldl, N., & Bilham, R. (2006). Great Himalayan earthquakes and the Tibetan plateau. *Nature*, *444*(7116), 165–170. https://doi.org/10.1038/nature05199

Fischer, T., Horálek, J., Hrubcová, P., Vavrycuk, V., Bräuer, K., & Kämpf, H.(2014). Intra-continental earthquake swarms in West-Bohemia and Vogtland: A review. *Tectonophysics*, *611*, 1–27. https://doi.org/10.1016/j.tecto.2013.11.001

Gardonio, B., Jolivet, R., Calais, E., & Leclère, H. (2018). The April 2017 M_w6.5 Botswana earthquake: An intraplate event triggered by deep fluids. *Geophysical Research Letters*, *45*, 8886–8896. https://doi.org/10.1029/2018GL078297

Grollimund, B., & Zoback, M. D. (2001). Did deglaciation trigger intraplate seismicity in the New Madrid Seismic Zone? *Geology*, *29*(2), 175–178.

Guo, L., Magnani, M. B., McIntosh, K., & Waldron, B. (2014). Quaternary deformation and fault structure in the Northern Mississippi Embayment as imaged by near-surface seismic reflection data. *Tectonics*, *33*, 807–823. https://doi.org/10.1002/2013TC003464

Hainzl, S., Kraft, T., Wassermann, J., Igel, H., & Schmedes, E. (2006). Evidence for rainfall-triggered earthquake activity. *Geophysical Research Letters*, *33*, L19303. https://doi.org/10.1029/2006GL027642

Han, L., Zhou, Y., He, C., & Li, H. (2016). Sublithostatic pore fluid pressure in the brittle-ductile transition zone of Mesozoic Yingxiu-Beichuan fault and its implication for the 2008 M_w 7.9 Wenchuan earthquake. *Journal of Asian Earth Sciences*, *117*, 107–118. https://doi.org/10.1016/j.jseaes.2015.12.009

Hao, Y., Magnani, M. B., McIntosh, K., Waldron, B., & Guo, L. (2013). Quaternary deformation along the Meeman-Shelby Fault near Memphis, Tennessee, imaged by high-resolution marine and land seismic reflection profiles. *Tectonics*, *32*, 501–515. https://doi.org/10.1002/tect.20042

Herrmann, R. B. (1979). Surface wave focal mechanisms for eastern North American earthquakes with tectonic implications. *Journal of Geophysical Research*, *84*, 3543–3552. https://doi.org/10.1029/JB084iB07p03543

Herrmann, R. B., & Ammon, C. J. (1997). Faulting parameters of earthquakes in the New Madrid, Missouri, region. *Engineering Geology*, *46*(3), 299–311. https://doi.org/10.1016/S0013-7952(97)00008-2

Herrmann, R. B., & Canas, J.-A. (1978). Focal mechanism studies in the New Madrid Seismic Zone. *Bulletin of the Seismological Society of America*, *68*(4), 1095–1102.

Heuer, B., Geissler, W. H., Kind, R., & Kampf, H. (2006). Seismic evidence for asthenospheric updoming beneath the western Bohemian Massif, central Europe. *Geophysical Research Letters*, *33*, L05311. https://doi.org/10.1029/2005GL025158

Hildebrand, R. S., & Easton, R. M. (1995). An 1161 Ma suture in the Frontenac terrane, Ontario segment of the Grenville orogen. *Geology*, *23*(10), 917–920. https://doi.org/10.1130/0091-7613(1995)023<0917:AMSITF>2.3.CO;2

Holbrook, J., Autin, W. J., Rittenour, T. M., Marshak, S., & Goble, R. J. (2006). Stratigraphic evidence for millennial-scale temporal clustering of earthquakes on a continental-interior fault: Holocene Mississippi River floodplain deposits, New Madrid seismic zone, USA. *Tectonophysics*, *420*(3), 431–454. https://doi.org/10.1016/j.tecto.2006.04.002

Hough, S. E., Armbruster, J. G., Seeber, L., & Hough, J. E. (2000). On the, odified Mercalli intensities and magnitudes of the 1811–1812 New Madrid earthquakes. *Journal of Geophysical Research*, *105*, 23,839–23,864. https://doi.org/10.1029/2000JB900110

Hough, S. E., & Page, M. (2011). Toward a consistent model for strain accrual and release for the New Madrid Seismic Zone, central United States. *Journal of Geophysical Research*, *116*, B03311. https://doi.org/10.1029/2010jb007783

Hurd, O., & Zoback, M. D. (2012). Regional stress orientations and slip compatibility of earthquake focal planes in the New Madrid Seismic Zone. *Seismological Research Letters*, *83*(4), 672–679. https://doi.org/10.1785/0220110122

Johnson, G. A., Horton, S. P., Withers, M., & Cox, R. (2014). Earthquake focal mechanisms in the New Madrid Seismic Zone. *Seismological Research Letters*, *85*(2), 257–267. https://doi.org/10.1785/0220130140

Johnston, A. C. (1989). The seismicity of stable continental interiors, *Earthquakes at North-Atlantic passive margins: Neotectonics and postglacial rebound* (pp. 299–327). Netherlands, Dordrecht: Springer. https://doi.org/10.1007/978-94-009-2311-9-18

Johnston, A. C., & Schweig, E. S. (1996). The enigma of the New Madrid earthquakes of 1811–1812. *Annual Review of Earth and Planetary Sciences*, *24*(1), 339–384. https://doi.org/10.1146/annurev.earth.24.1.339

Kennedy, B. M., & Soest, M. C. v. (2007). Flow of mantle fluids through the ductile lower crust: Helium isotope trends. *Science*, *318*(5855), 1433–1436. https://doi.org/10.1126/science.1147537

Kenner, S. J., & Segall, a. P. (2000). A mechanical model for intraplate earthquakes: Application to the New Madrid Seismic Zone. *Science*, *289*(5488), 2329–2332. https://doi.org/10.1126/science.289.5488.2329

Keranen, K. M., & Weingarten, M. (2018). Induced seismicity. *Annual Review of Earth and Planetary Sciences*, *46*(1), 149–174. https://doi.org/10.1146/annurev-earth-082517-010054

Küster, M., & Stöckhert, B. (1999). High differential stress and sublithostatic pore fluid pressure in the ductile regime—Microstructural evidence for short-term post-seismic creep in the Sesia Zone, Western Alps. *Tectonophysics*, *303*(1), 263–277. https://doi.org/10.1016/S0040-1951(98)00256-X

Leclère, H., & Fabbri, O. (2013). A new three-dimensional method of fault reactivation analysis. *Journal of Structural Geology*, *48*, 153–161. https://doi.org/10.1016/j.jsg.2012.11.004

Leclère, H., Lacroix, B., & Fabbri, O. (2014). Fault mechanics at the base of the continental seismogenic zone: Insights from geochemical and mechanical analyses of a crustal-scale transpressional fault from the Argentera crystalline massif, French-Italian Alps. *Journal of Structural Geology*, *66*, 115–128. https://doi.org/10.1016/j.jsg.2014.05.009

Levandowski, W., Boyd, O. S., & Ramirez-Guzmán, L. (2016). Dense lower crust elevates long-term earthquake rates in the New Madrid Seismic Zone. *Geophysical Research Letters*, *43*, 1–12. https://doi.org/10.1002/2016GL070175

Levandowski, W., Herrmann, R. B., Briggs, R., Boyd, O., & Gold, R. (2018). An updated stress map of the continental United States reveals heterogeneous intraplate stress. *Nature Geoscience*, *11*(6), 433–437. https://doi.org/10.1038/s41561-018-0120-x

Li, Y.-G., Vidale, J. E., Aki, K., Xu, F., & Burdette, T. (1998). Evidence of shallow fault zone strengthening after the 1992 *M*7.5 Landers, California, earthquake. *Science*, *279*(5348), 217–219. https://doi.org/10.1126/science.279.5348.217

Liu, M., Stein, S., & Wang, H. (2011). 2000 years of migrating earthquakes in North China: How earthquakes in midcontinents differ from those at plate boundaries. *Lithosphere*, *3*(2), 128–132.

Marone, C. (1998). The effect of loading rate on static friction and the rate of fault healing during the earthquake cycle. *Nature*, *391*(6662), 69–72. https://doi.org/10.1038/34157

Martin, P., Arroucau, P., & Vlahovic, G. (2014). Shear-wave splitting study of crustal anisotropy in the New Madrid Seismic Zone. *Bulletin of the Seismological Society of America*, *104*(3), 1100–1110. https://doi.org/10.1785/0120130222

Mittempergher, S., Dallai, L., Pennacchioni, G., Renard, F., & Di Toro, G. (2014). Origin of hydrous fluids at seismogenic depth: Constraints from natural and experimental fault rocks. *Earth and Planetary Science Letters*, *385*, 97–109. https://doi.org/10.1016/j.epsl.2013.10.027

Mooney, W. D., Andrews, M. C., Ginzburg, A., Peters, D. A., & Hamilton, R. M. (1983). Crustal structure of the <orthern Mississippi embayment and a comparison with other continental rift zones. *Tectonophysics*, *94*(1), 327–348. https://doi.org/10.1016/0040-1951(83)90023-9

Moore, D. E., & Lockner, D. A. (2004). Crystallographic controls on the frictional behavior of dry and water-saturated sheet structure minerals. *Journal of Geophysical Research*, *109*, B03401. https://doi.org/10.1029/2003JB002582

Moore, D. E., & Rymer, M. J. (2007). Talc-bearing serpentinite and the creeping section of the San Andreas fault. *Nature*, *448*(7155), 795–797 . https://doi.org/10.1038/nature06064

Morris, A., Ferrill, D. A., & Henderson, D. B. (1996). Slip-tendency analysis and fault reactivation. *Geology*, *24*(3), 275–278. https://doi.org/10.1130/0091-7613(1996)024<0275:STAAFR>2.3.CO;2

Mueller, K., Hough, S. E., & Bilham, R. (2004). Analysing the 1811–1812 New Madrid earthquakes with recent instrumentally recorded aftershocks. *Nature*, *429*(6989), 284–288. https://doi.org/10.1038/nature02557

Nelson, K., & Zhang, J. (1991). A COCORP deep reflection profile across the buried Reelfoot Rift, South-Central United States. *Tectonophysics*, *197*(2-4), 271–293. https://doi.org/10.1016/0040-1951(91)90046-U

Nocquet, J.-M. (2012). Present-day kinematics of the Mediterranean: A comprehensive overview of GPS results. *Tectonophysics*, *579*, 220–242. https://doi.org/10.1016/j.tecto.2012.03.037

Nuttli, O. W. (1973). The Mississippi Valley earthquakes of 1811 and 1812: Intensities, ground motion and magnitudes. *Bulletin of the Seismological Society of America*, *63*(1), 227–248.

Nyamwandha, C. A., Powell, C. A., & Langston, C. A. (2016). A joint local and teleseismic tomography study of the Mississippi Embayment and New Madrid Seismic Zone. *Journal of Geophysical Research: Solid Earth*, *121*, 3570–3585. https://doi.org/10.1002/2015JB012761

Page, M. T., & Hough, S. E. (2014). The New Madrid Seismic Zone: Not dead yet. *Science*, *343*(6172), 762–764. https://doi.org/10.1126/science.1248215

Pollitz, F. F., & Mooney, W. D. (2014a). Seismic structure of the Central US crust and shallow upper mantle: Uniqueness of the Reelfoot Rift. *Earth and Planetary Science Letters*, *402*, 157–166.

Pollitz, F. F., & Mooney, W. D. (2014b). Seismic structure of the Central US crust and shallow upper mantle: Uniqueness of the Reelfoot Rift. *Earth and Planetary Science Letters*, *402*, 157–166. https://doi.org/10.1016/j.epsl.2013.05.042

Powell, C. A., Withers, M. M., DeShon, H. R., & Dunn, M. M. (2010). Intrusions and anomalous Vp/Vs ratios associated with the New Madrid seismic zone. *Journal of Geophysical Research*, *115*, B08311. https://doi.org/10.1029/2009JB007107

Quinones, L. A., DeShon, H. R., Magnani, M. B., & Frohlich, C. (2018). Stress orientations in the Fort Worth Basin, Texas, determined from earthquake focal mechanisms stress orientations in the Fort Worth Basin. *Bulletin of the Seismological Society of America*, *108*(3A), 1124–1132. https://doi.org/10.1785/0120170337

Rice, J. R. (1992). Chapter 20 fault stress states, pore pressure distributions, and the weakness of the San Andreas Fault. In B. Evans, & T.-F. Wong (Eds.), *Fault Mechanics and Transport Properties of Rocks - A Festschrift in Honor of W. F. Brace* (Vol. 51, pp. 475–503). https://doi.org/10.1016/s0074-6142(08)62835-1

Rigo, A., Béthoux, N., Masson, F., & Ritz, J.-F. (2008). Seismicity rate and wave-velocity variations as consequences of rainfall: The case of the catastrophic storm of September 2002 in the Nîmes Fault region (Gard, France). *Geophysical Journal International*, *173*(2), 473–482. https://doi.org/10.1111/j.1365-246X.2008.03718.x

Rittenour, T. M., Blum, M. D., & Goble, R. J. (2007). Fluvial evolution of the lower Mississippi River valley during the last 100 k.y. glacial cycle: Response to glaciation and sea-level change. *GSA Bulletin*, *119*(5-6), 586–608. https://doi.org/10.1130/B25934.1

Shimamoto, T. (1986). Strengthening of phyllosilicate and gypsum gouges with increasing temperature: Effect of temperature or moisture elimination? *International Journal of Rock Mechanics and Mining Sciences & Geomechanics Abstracts*, *23*(6), 439–443. https://doi.org/10.1016/0148-9062(86)92309-0

Shumway, A. M. (2008). Focal mechanisms in the Northeast New Madrid Seismic Zone. *Seismological Research Letters*, *79*(3), 469–477. https://doi.org/10.1785/gssrl.79.3.469

Sibson, R. H. (1985). A note on fault reactivation. *Journal of Structural Geology*, *7*(6), 751–754. https://doi.org/10.1016/0191-8141(85)90150-6

Sibson, R. H. (2014). Earthquake rupturing in fluid-overpressured crust: How common? *Pure and Applied Geophysics*, *171*(11), 2867–2885. https://doi.org/10.1007/s00024-014-0838-3

Sleep, N. H., & Blanpied, M. L. (1992). Creep, compaction and the weak rheology of major faults. *Nature*, *359*(6397), 687–692. https://doi.org/10.1038/359687a0

Smalley, R., Ellis, M. A., Paul, J., & Van Arsdale, R. B. (2005). Seismology: Tectonic strain in plate interiors? (Reply) *Nature*, *438*(7070), 10. https://doi.org/10.1038/nature04429

Stein, S., & Liu, M. (2009). Long aftershock sequences within continents and implications for earthquake hazard assessment. *Nature*, *462*(7269), 87–89. https://doi.org/10.1038/nature08502

Streit, J. E. (1999). Conditions for earthquake surface rupture along the San Andreas fault System, California. *Journal of Geophysical Research*, *104*, 17,929–17,939. https://doi.org/10.1029/1999JB900131

Thomas, W. A. (2014). A mechanism for tectonic inheritance at transform faults of the Iapetan margin of Laurentia. *Geoscience Canada*, *41*(3), 321–344.

Thomas, A. M., Nadeau, R. M., & Bürgmann, R. (2009). Tremor-tide correlations and near-lithostatic pore pressure on the deep San Andreas fault. *Nature*, *462*(7276), 1048–1051. https://doi.org/10.1038/nature08654

Thomas, W. A., & Powell, C. A. (2017). Necessary conditions for intraplate seismic zones in North America. *Tectonics*, *36*, 2903–2917. https://doi.org/10.1002/2017TC004502

Townend, J., & Zoback, M. D. (2000). How faulting keeps the crust strong. *Geology*, *28*(5), 399–402. https://doi.org/10.1130/0091-7613(2000)28<399:HFKTCS>2.0.CO;2

Tregoning, P., Burgette, R., McClusky, S. C., Lejeune, S., Watson, C. S., & McQueen, H. (2013). A decade of horizontal deformation from great earthquakes. *Journal of Geophysical Research: Solid Earth*, *118*, 2371–2381. https://doi.org/10.1002/jgrb.50154

Tuttle, M. P., Schweig, E. S., Sims, J. D., Lafferty, R. H., Wolf, L. W., & Haynes, M. L. (2002). The earthquake potential of the New Madrid Seismic Zone. *Bulletin of the Seismological Society of America*, *92*(6), 2080–2089. https://doi.org/10.1785/0120010227

Van Arsdale, R. (2000). Displacement history and slip rate on the Reelfoot fault of the New Madrid Seismic Zone. *Engineering Geology*, *55*(4), 219–226. https://doi.org/10.1016/S0013-7952(99)00093-9

Van Schmus, W. R., Bickford, M. E., & Turek, A. (1996). Proterozoic geology of the east-central Midcontinent basement. In B. A. van der Pluijm, & P. A. Catacosinos (Eds.), *Basement and basins of eastern North America*. https://doi.org/10.1130/0-8137-2308-6.7

Wehrens, P., Berger, A., Peters, M., Spillmann, T., & Herwegh, M. (2016). Deformation at the frictional-viscous transition: Evidence for cycles of fluid-assisted embrittlement and ductile deformation in the granitoid crust. *Tectonophysics*, *693*, 66–84. https://doi.org/10.1016/j.tecto.2016.10.022

Weise, S. M., Bräuer, K., Kämpf, H., Strauch, G., & Koch, U. (2001). Transport of mantle volatiles through the crust traced by seismically released fluids: A natural experiment in the earthquake swarm area Vogtland/NW Bohemia Central Europe. *Tectonophysics*, *336*(1), 137–150. https://doi.org/10.1016/S0040-1951(01)00098-1

Wu, P., & Johnston, P. (2000). Can deglaciation trigger earthquakes in N. America? *Geophysical Research Letters*, *29*, 1321–1326.

Xu, H., Xu, S., Nieto-Samaniego, N. F., & Alaniz-Alvarez, S. A. (2017). Slicken 1.0: Program for calculating the orientation of shear on reactivated faults. *Computers & Geosciences*, *104*, 158–165. https://doi.org/10.1016/j.cageo.2016.07.015

Xue, L., Li, H.-B., Brodsky, E. E., Xu, Z.-Q., Kano, Y., Wang, H., et al. (2013). Continuous permeability measurements record healing inside the Wenchuan earthquake fault zone. *Science*, *340*(6140), 1555–1559. https://doi.org/10.1126/science.1237237

Yukutake, Y., Ito, H., Honda, R., Harada, M., Tanada, T., & Yoshida, A. (2011). Fluid-induced swarm earthquake sequence revealed by precisely determined hypocenters and focal mechanisms in the 2009 activity at Hakone volcano, Japan. *Journal of Geophysical Research*, *116*, B04308. https://doi.org/10.1029/2010JB008036

Zhan, Y., Hou, G., Kusky, T., & Gregg, P. M. (2016). Stress development in heterogenetic lithosphere: Insights into earthquake processes in the New Madrid Seismic Zone. *Tectonophysics*, *671*, 56–62.